

Design of Underactuated Steerable Electrode Arrays for Optimal Insertions

Jian Zhang

e-mail: jz2181@columbia.edu

Nabil Simaan¹

e-mail: nabil.simaan@vanderbilt.edu

Advanced Robotics and Mechanisms
Applications Lab (ARMA Lab),
Department of Mechanical Engineering,
Vanderbilt University,
Nashville, TN 37235

This paper addresses the design of wire actuated steerable electrode arrays for optimal insertions in cochlear implant surgery. These underactuated electrode arrays are treated as continuum robots which have an embedded actuation strand inside their flexible medium. By pulling on the actuation strand, an electrode array assumes a minimum-energy shape. The problems of designing optimal actuation strand placement are addressed in this paper. Based on the elastic modeling of the steerable electrode arrays proposed in this paper, an analytical solution of the strand placement is solved to minimize the shape discrepancy between a bent electrode array and a given target curve defined by the anatomy. Using the solved strand placement inside the steerable electrode array, an optimized insertion path planning with robotic assistance is proposed to execute the insertion process. Later, an optimization algorithm is presented to minimize the shape discrepancy between an inserted electrode array and a given target curve during the whole insertion process. Simulations show a steerable electrode array bending using the elastic model and robot insertion path planning with optimized strand placement. Two experiments have been conducted to validate the elastic model and algorithms.

[DOI: 10.1115/1.4007005]

1 Introduction and Clinical Motivation

Cochlear implant surgery restores partial hearing for patients suffering from severe hearing loss, but with intact hair cells. During surgery, surgeons insert a flexible electrode array (EA) into the scala tympani—a helical chamber inside the cochlea shown in Fig. 1. This insertion process can be traumatic if the EA perforates the basilar membrane or obliterates the fragile intracochlear anatomy [1–9].

In an effort to reduce intracochlear trauma, and to improve electrode positioning, surgeons have been testing various insertion techniques and many different designs of EAs. Existing EA designs try to minimize intracochlear trauma by making the EA smaller, more compliant, or shorter [10–13]. However, with reduced size and increased compliance, the EAs become more flimsy and less controllable. Shortening the EAs reduces potential trauma, but prohibits access to the deeper ganglion cells associated with restoration of lower frequencies of sound.

Two basic types of EAs exist: external-wall straight EAs (e.g., C40+ from MEDEL) and perimodiolar EAs (e.g., Contour Advance from Cochlear Inc, and HiFocus Helix from Advanced Bionics). External-wall electrodes passively slide on the outer wall of the cochlea during insertion. Roland [8] showed that external-wall electrodes have the disadvantage of increased tendency to slide up and push against the basilar membrane. Perimodiolar EAs require an internal stylet or an external sheath to straighten their distal end during insertion. These electrodes passively bend in predetermined shapes as they slide off the stylet or out of the external sheath during insertions. They thus reduce contact with the outer walls of the scala tympani and position the electrodes closer to the auditory nerves. This has been shown in Ref. [14] to reduce excitation current thresholds and corresponding cross-talk among adjacent electrodes. Recently, sensors for gauging the bending angle of the EA have been developed [15,16].

Despite these advances in EA design, current electrodes do not provide active controllable steerability and lack force feedback. Current tools used by surgeons require substantial training to achieve proper atraumatic insertions. Typical insertion forces are less than 10 g [8], which further complicates the decision making process of choosing a safe insertion depth at which electrode insertion should stop in order to avoid potential trauma. It also has been recently shown in Ref. [17] that the insertion speed has a non-negligible impact on reducing electrode insertion forces.

To overcome these limitations of cochlear implant surgery, a novel concept of robotically assisted cochlear implant surgery using steerable EAs has been put forth in Ref. [18]. Later, Refs. [19] and [20] proposed a similar robotic tool for electrode insertions. Our proposed design of the steerable EAs in Ref. [18] uses an actuation strand placed inside the flexible medium of the EA, Fig. 2(a). This design was inspired by other designs for steerable continuum robots as previously presented in Ref. [21]. A similar design with embedded shape memory alloy was later proposed in Ref. [22].

The choice of this rather simplistic design was motivated by the limited available space (typical cross section diameters of cochlear implant EAs range between 400 μm at the tip and 1200 μm at the base). In addition, proximity to the auditory nerve limits the use of electrical actuation due to difficulty of insulating the electrically sensitive anatomy [23] and complications of shielding individual electrode wires from electrical noise generated by the electrode actuation lines.

Controllable bending of the EA is limited to equilibrium shapes. These shapes are defined by minimum-energy conditions [21,24–26]. Given a particular positioning of the actuation strand inside the elastomeric medium, one can experimentally calibrate a kinematic model for the EA by robotically pulling a known amount on the actuation strand and characterizing the resulting equilibrium shape. When pulling on the strand, manually or robotically, the electrode array is inserted in a coordinated motion, which is described in Sec. 4.3. In Refs. [18] and [27], we used manual digitization of points along the backbone curve. In Ref. [28], we used automatic segmentation of electrode edges and spline curve fitting to characterize the resulting equilibrium shapes of the electrode. Regardless of the method used, experimental

¹Corresponding author.

Contributed by the Mechanisms and Robotics Committee of ASME for publication in the JOURNAL OF MECHANISMS AND ROBOTICS. Manuscript received March 7, 2011; final manuscript received April 25, 2012; published online January 24, 2013. Assoc. Editor: Anupam Saxena.

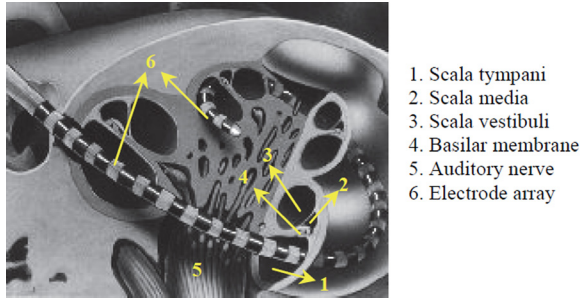


Fig. 1 Insertion of electrode arrays into the scala tympani

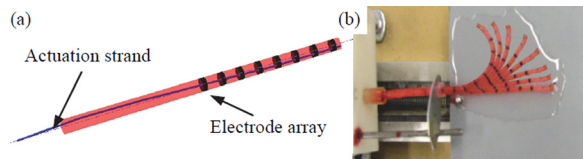


Fig. 2 (a) Top and side view of the steerable electrode array with embedded strand, (b) bent shapes of the steerable electrode array

calibration has the advantage of providing accurate kinematic models that are independent of knowing the location of the actuation strand inside the flexible medium. However, the lack of modeling framework that can simulate the effects of different strand placements on the bending equilibrium shapes of the EA limits the extent to which EA insertions can be optimized. Such modeling framework is essential for comprehensive optimization of strand placement inside the EA and the insertion path plans.

In this paper, an elastic model of the steerable EAs is presented. Using this model, the steerable electrode calibration process is significantly simplified. Meanwhile, given a target curve of a certain length, we provide an analytical solution of the strand placement inside the EA to achieve desired bent shapes. Based on the determined strand placement, we briefly review our earlier work on robot path planning algorithms that control steerable EAs during insertions while minimizing the shape discrepancy between the bent steerable EA and the scala tympani [27], Fig. 1. Then, we propose a strand placement optimization algorithm that minimizes the shape discrepancy throughout the whole insertion process. We also propose and demonstrate the validity of planar placement of actuation strands that greatly simplify steerable EA manufacturing constraints.

Table 1 shows a comparison of our previous work with the analytical strand placement and the optimization algorithm presented in this paper. Our previous work only focused on robot path planning due to the fact that the strand is empirically placed inside the steerable EA. Analytical solution of the strand placement solves for the desired strand inside the EAs given a target curve. The optimization algorithm considers the robot path planning as part of the strand placement optimization and therefore generates the best strand placement that works throughout the whole insertion process.

The contributions of this paper include providing a comprehensive modeling and simulation framework for automatically cali-

Table 1 Different levels of optimization

	Robot path planning	Strand placement	Whole insertion process strand placement optimization
Earlier work [1]	Yes	No	No
Analytical solution	Yes	Yes	No
Optimization algorithm	Yes	Yes	Yes

brating and evaluating different steerable electrode designs. The paper uses this elastic model to derive an analytical solution of the desired strand given a target curve shape. Optimality of the electrode design is measured by an integral performance measure that quantifies the shape discrepancies between the bent steerable EA and the shape of the anatomy (target curve). Based on the elastic modeling, a strand placement optimization algorithm is proposed.

The theoretical problem addressed by this work is also related to other efforts in medical robotics such as works on the design and insertion of steerable cannulas. In Ref. [29], accurate modeling and resolved rates control of steerable cannula robots were presented. Equilibrium conformation modeling has also been presented in Ref. [30], while the path planning for insertion of concentric tube robots along anatomical paths has been presented in Ref. [31]. Other works on steering of beveled tip needles such as Ref. [32] focused on changing the rotation angle and speed of insertion of a beveled tip needle, kinematic-based path planning [33] or steering by changing boundary conditions [34].

While these works are somewhat relevant to this contribution, a uniform methodology for the optimal design and path planning of steerable underactuated elastomeric robots remains unsolved. This paper tries to address this limitation with a simplified problem of an elastomeric steerable robot within the context of cochlear implant surgery. The difference in our approach is that both path planning and optimal design of the underactuated robot are addressed in a single framework. However, our contribution does not address the design of steerable cannula robots as they have additional design constraints outside the scope of this work.

Despite the scope limitations of our work, we present a general design methodology and the necessary background for robotic insertion for steerable EAs. These steerable EAs are relevant for cochlear implants, neurosurgery (deep brain implants) or spinal implant surgery and for developing patient-specific EAs.

2 Nomenclature and Problem Statement

The Nomenclature and Figs. 3 and 4 show the symbols used throughout this paper. We also make the following modeling assumptions:

- (1) The steerable EA has a cross sectional symmetry if the hole at strand location is not considered. The actuation strand is

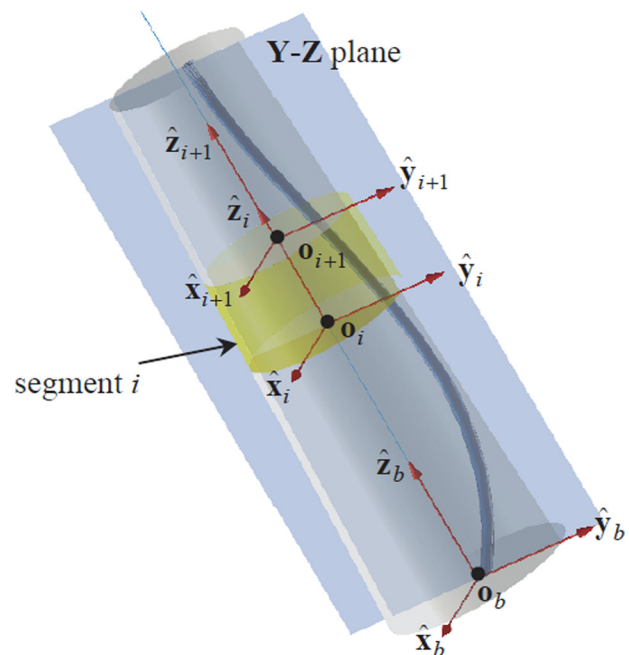


Fig. 3 Geometric modeling of the steerable electrode array in initial straight configuration with segment *i* highlighted

placed in the central plane of the EA and the EA bends in this plane.

- (2) The radial position increment of the strand between adjacent segments is negligible compared to the layer thickness.
- (3) The EA is linear elastic while the actuation strand is inextensible.
- (4) The distributed internal friction force per unit length between the elastomer and the actuation strand is assumed constant. The gap between the actuation strand and the surrounding elastomer is negligible.
- (5) The target curve and its first-order derivative are continuous.

The following three problems are addressed in this paper:

Problem 1: Given the location w_i of the actuation strand, find the equilibrium electrode shape $[\delta_i \ \varphi_{\text{eix}}]$ for a specified amount of pull q_1 on the strand or a specified force f_i on the actuation strand, where δ_i and φ_{eix} represent the deformation and bending angle of segment i .

Problem 2: Given a target curve shape $\theta_c(s)$ of length (insertion depth) d to be approximated by the electrode, find the optimal w_i that minimizes this shape discrepancy for insertion depth d .

Problem 3: Given a target shape $\theta_c(s)$ to be approximated by the EA throughout the whole insertion process, find the optimal w_i that minimizes the averaged shape discrepancies throughout the whole electrode insertion process.

3 Elastic Modeling of Steerable Electrode Arrays

3.1 Modeling of the Initial Strand Placement. The steerable EA is geometrically modeled as a long beam with length u , Fig. 3. We discretize the electrode using n segments indexed by i . These segments are for modeling purpose rather than physical segments since the electrode array is made of a continuous elastomer. The segment thickness is given by $ds = u/n$. For segment i ($i = 1 \dots n$), we setup the following coordinate systems. The electrode base frame $\{\mathbf{o}_b\}$ is aligned with the world frame. The origin of $\{\mathbf{o}_b\}$ is defined at the geometric center of the base cross section. The \hat{z}_b axis is defined along the axis of the EA in a straight configuration. The \hat{x}_b and \hat{y}_b axes are arbitrarily defined. In addition, we define local segment frames $\{\mathbf{o}_i\}$, located at the geometric centers of the bottom cross sections of segment i , Fig. 3. Axes \hat{y}_i are defined along the direction from \mathbf{o}_i to the strand location w_i at the bottom cross section of segment i . Axis \hat{z}_i is perpendicular to the bottom surface of segment i and passes through \mathbf{o}_i . Axis \hat{x}_i completes $\{\mathbf{o}_i\}$ to form a right-handed frame $\hat{x}_i = \hat{y}_i \times \hat{z}_i$. In Fig. 3, $\{\mathbf{o}_1\}$ coincides with $\{\mathbf{o}_b\}$.

Coordinate w_{iy} is used to define the initial strand placement when the electrode is fully straight and there is no force acting on the actuation strand. In local coordinate $\{\mathbf{o}_i\}$, the strand location is given by ${}^{(i)}\mathbf{w}_i = [0 \ w_{iy} \ 0]^T$ since the strand passes along axis \hat{y}_i . The strand location at the top surface of segment i is given by ${}^{(i)}\mathbf{w}_{i+1}$ in frame $\{\mathbf{o}_i\}$

$${}^{(i)}\mathbf{w}_{i+1} = \mathbf{I}^{(i+1)}\mathbf{w}_{i+1} + {}^{(i)}\mathbf{o}_{i+1} \quad (1)$$

Table 2 Global optimization results

Simulation conditions		$\bar{\theta}_l$ (deg)
Analytical solution	Unsmoothed strand placement	24.180
	Smoothed linear strand placement	20.111
Linear cases	The best result from global search	19.318
	Second best result from global search	19.432
	Result from optimization algorithm	19.677
	Third best result from global search	19.963
Nonlinear cases	Result from optimization algorithm	19.470
	The best result from global search	20.716

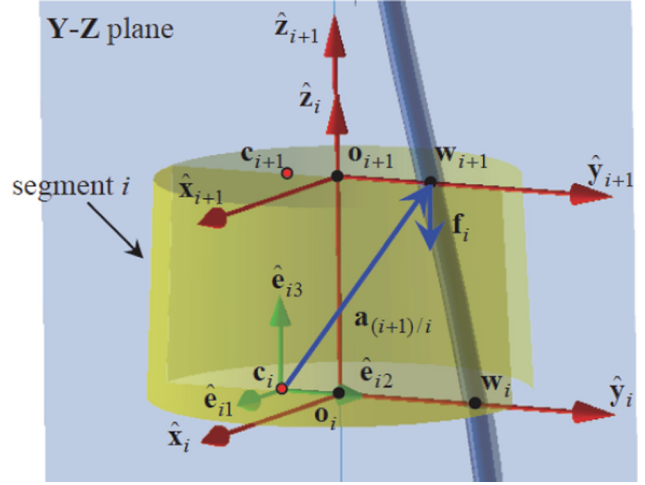


Fig. 4 Static modeling of the steerable electrode array at layer i

Therefore, the initial strand placement is fully defined given the coordinates w_{iy} for all segments $i = 1 \dots n$.

3.2 Elastic Modeling of the Bent Electrode Array. Define \mathbf{c}_i as the centroid of the bottom cross section of segment i , Fig. 4. This centroid is calculated according to Eq. (2) while accounting for the diameter of the strand d_w

$${}^{(i)}\mathbf{c}_i = \frac{{}^{(i)}\mathbf{o}_i A_i - \frac{1}{4} {}^{(i)}\mathbf{w}_i \pi d_w^2}{A_i - \frac{1}{4} \pi d_w^2} \quad (2)$$

Based on the definition of frame $\{\mathbf{o}_i\}$, ${}^{(i)}\mathbf{c}_i$ is always on the \hat{y}_i axis. Therefore, ${}^{(i)}\mathbf{c}_i = [0 \ c_{iy} \ 0]^T$. In Fig. 4, the EA has circular cross sections with a diameter of d_{ei} at segment i , ${}^{(i)}\mathbf{c}_i$ simplifies to

$${}^{(i)}\mathbf{c}_i = \frac{{}^{(i)}\mathbf{o}_i d_{ei}^2 - {}^{(i)}\mathbf{w}_i d_w^2}{d_{ei}^2 - d_w^2} \quad (3)$$

In a scalar form

$$c_{iy} = \frac{-d_w^2}{d_{ei}^2 - d_w^2} w_{iy}$$

The magnitude of the total pulling force on the strand at the base of the electrode is designated by f_i . The force of the strand decreases along the length of the electrode due to distributed internal friction. Let α_f be the internal friction per a unit length. The pulling force acting on segment i is given by

$$\mathbf{f}_i = (f_i - \alpha_f i ds) \hat{\mathbf{n}}_i \quad (4)$$

where $\hat{\mathbf{n}}_i$ is a unit vector along negative \hat{z}_i direction because of assumption 0. This force \mathbf{f}_i results in a moment \mathbf{m}_i and an axial force on segment i . The bending moment is given by

$$\mathbf{m}_i = \mathbf{a}_{i+1/i} \times \mathbf{f}_i \quad (5)$$

where $\mathbf{a}_{i+1/i}$ is the vector from \mathbf{c}_i to \mathbf{w}_{i+1} in Fig. 4.

Since the cross sections of the electrode are symmetric about \hat{y}_i , the principal axes of bending remain parallel to frame $\{\mathbf{o}_i\}$ and pass through \mathbf{c}_i .

Each segment undergoes axial shrinkage and bending. Define δ_i as the axial deflection of segment i , φ_{eix} as the bending angle about an axis $\hat{\mathbf{e}}_{i1}$ parallel to \hat{x}_i axis and passing through \mathbf{c}_i .

The deflections of segment i are calculated using its axial and bending stiffnesses. The axial stiffness is given by $k_i = EA_i/ds$ and the bending stiffness components are given by $k_{\varphi_{ix}}$

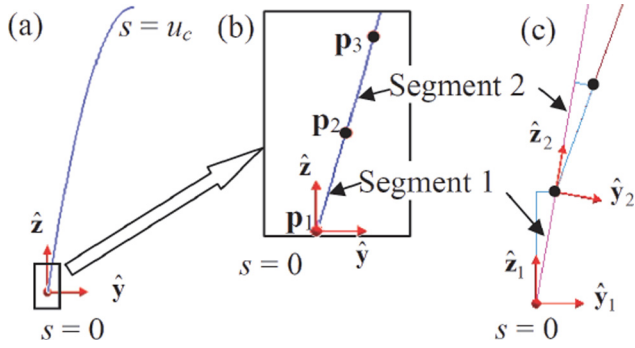


Fig. 5 (a) Target curve, (b) segmented target curve, and (c) local coordinate systems of the bent steerable electrode array

$= EI_i^{xx}/ds$, where I_i^{xx} is the second moment of area about axes \hat{e}_{i1} . The second moment of inertia is given by the parallel axes theorem

$$I_i^{xx} = \left(\frac{\pi d_{ei}^4}{64} + \frac{\pi d_{ei}^2}{4} c_{iy}^2 \right) - \left(\frac{\pi d_w^4}{64} + \frac{\pi d_w^2}{4} (w_{iy} - c_{iy})^2 \right) \quad (6)$$

The axial deflections of each segment and the bending about \hat{e}_{i1} are calculated via the compliance matrix of the segment

$$\begin{bmatrix} \delta_i \\ \varphi_{eix} \end{bmatrix} = \mathbf{C}_i \begin{bmatrix} \hat{z}_i^T & \mathbf{0} \\ \mathbf{0} & \hat{x}_i^T \end{bmatrix} \begin{bmatrix} \mathbf{f}_i \\ \mathbf{m}_i \end{bmatrix} \quad (7)$$

where $\mathbf{C}_i = \text{diag}(ds/EA_i, ds/EI_i^{xx})$.

Given the deflections, the orientation of the top section of the segment i may be described with respect to $\{\mathbf{o}_i\}$ by

$$\mathbf{D}_i = e^{\hat{e}_{i1} \varphi_{eix}} \quad (8)$$

where \hat{e}_{i1} , \hat{e}_{i2} , and \hat{e}_{i3} are the standard basis unit vectors for the principal axes of frame $\{\mathbf{o}_i\}$. The new location of the origin of frame $\{\mathbf{o}_{i+1}\}$ is given by the axial shrinkage and the rotation \mathbf{D}_i

$${}^{(i)}\mathbf{o}_{i+1} = {}^{(i)}\mathbf{c}_i + \mathbf{D}_i \left((ds + \delta_i) {}^{(i)}\hat{z}_i - {}^{(i)}\mathbf{c}_i \right) \quad (9)$$

The orientation and position of any segment of the deformed electrode can be found by

$${}^0\mathbf{R}_i = \prod_{k=0}^{i-1} {}^k\mathbf{R}_{k+1} \quad \text{where } {}^{i-1}\mathbf{R}_i = \mathbf{D}_i \quad (10)$$

$${}^{(0)}\mathbf{o}_i = \sum_{k=0}^{i-1} {}^0\mathbf{R}_k {}^{(k)}\mathbf{o}_{k+1} \quad \text{where } {}^{(0)}\mathbf{o}_1 = \mathbf{0} \quad (11)$$

4 Optimized Strand Placement

4.1 Analytical Solution. Equation (7) provides the solution for the deflections of all the segments of the EA given the total actuation force on the strand and the location of the strand inside the flexible medium. This section solves problem 2 defined in Sec. 2 and provides an analytical solution, i.e., given a certain target curve with length d (insertion depth d), find the optimal \mathbf{w}_i that minimizes the shape discrepancies between the bent steerable EAs and the target curve at insertion depth d .

Based on assumption 0, the explicit form of Eq. (9) is given by

$${}^{(i)}\mathbf{o}_{i+1} = \left[0, \quad -\varphi_{eix}(ds + \delta_i), \quad \frac{d_w^2 w_{iy} \varphi_{eix}}{d_{ei}^2 - d_w^2} + (ds + \delta_i) \right]^T \quad (12)$$

where the location of ${}^{(i)}\mathbf{o}_{i+1}$ along electrode backbone includes $(ds + \delta_i)$ which is caused by shrinkage of the segment and φ_{eix} which is caused by the bending of the segment. Since the shrinkage $(ds + \delta_i)$ is only depend on the applied force, we use $(ds + \delta_i)$ as an estimated segment length between \mathbf{o}_i and \mathbf{o}_{i+1} to find the corresponding point \mathbf{p}_{i+1} on the target curve.

Figure 5(a) shows a target curve of length u_c ($u_c \geq u$). The analytical solution starts from the bottom (segment 1) of the EA. The estimated point \mathbf{p}_2 is first found by curve integral, such that

$$\overline{\mathbf{p}_1 \mathbf{p}_2} = ds + \delta_1 \quad (13)$$

where \mathbf{p}_1 coincides with the origin of the target curve.

Using Eq. (12) to match the desired ${}^{(1)}\mathbf{p}_2 = [0 \quad p_{2y} \quad p_{2z}]^T$ with ${}^{(1)}\mathbf{o}_2$ along \hat{y}_1 direction gives the following equation:

$$-\varphi_{e1x}(ds + \delta_1) = p_{2y} \quad (14)$$

By substituting Eqs. (7) in (14), the strand placement w_{1y} of segment 1 is obtained. Note that in Eq. (14), \mathbf{p}_2 needs to be expressed in local frame $\{\mathbf{o}_1\}$.

Once the strand placement in the first segment of the EA is solved, the above algorithm iteratively solves for the rest of the segments. To find a better estimated point \mathbf{p}_{i+1} , the arc length between \mathbf{p}_{i+1} and \mathbf{p}_i is updated by

$$\overline{\mathbf{p}_i \mathbf{p}_{i+1}} = \overline{\mathbf{o}_i \mathbf{o}_i} + (ds + \delta_i) \quad (15)$$

where $\overline{\mathbf{o}_i \mathbf{o}_i}$, ($i > 1$) is the actual arc length between \mathbf{o}_i and \mathbf{o}_i of the bent EA given by

$$\overline{\mathbf{o}_i \mathbf{o}_i} = \sum_{k=1}^{i-1} \| {}^{(i)}\mathbf{o}_{k+1} \| \quad (16)$$

This way, the optimal strand placement of all segments is solved recursively using Eq. (14).

4.2 Virtual Calibration Using the Elastic Model. In our previous work, for any fabricated steerable EAs, an experimental calibration process is needed to get its bending characteristics. In detail, the shape of the EA is represented by $\theta_e(s, q_1)$, where θ_e is the tangent angle at arc length s along its backbone given the actuation of the strand q_1 . The direct kinematics of the EA is approximated using the following modal representation [35]:

$$\theta_e(s, q_1) = \boldsymbol{\psi}(s)^T \mathbf{A} \boldsymbol{\eta}(q_1) \quad (17)$$

where $\boldsymbol{\psi}(s) = [1, s, s^2, \dots, s^{v-1}]^T$ and $\boldsymbol{\eta} = [1, q_1, q_1^2, \dots, q_1^{w-1}]^T$.

The experimental data matrix $\Phi_{ij} = \theta_e(s_i, q_{1j})$ is obtained by digitizing g equidistant points along its backbone in z different images of the EA as associated with z different values of q_1 , Fig. 6. In matrix form, the experimental matrix is expressed by

$$\Phi = \Omega_{g \times v} \mathbf{A}_{v \times w} \Gamma_{w \times z} \quad (18)$$

where

$$\Omega = \begin{bmatrix} 1 & s=0 & \dots & s=0^{v-1} \\ & & \vdots & \\ 1 & s=s_{\max} & \dots & s=s_{\max}^{v-1} \end{bmatrix}_{g \times v} \quad (19)$$

$$\Gamma = \begin{bmatrix} 1 & & & 1 \\ q_1 & & & q_{1 \max} \\ \vdots & \dots & & \vdots \\ q_1^{w-1} & & & q_{1 \max}^{w-1} \end{bmatrix}_{w \times z} \quad (20)$$

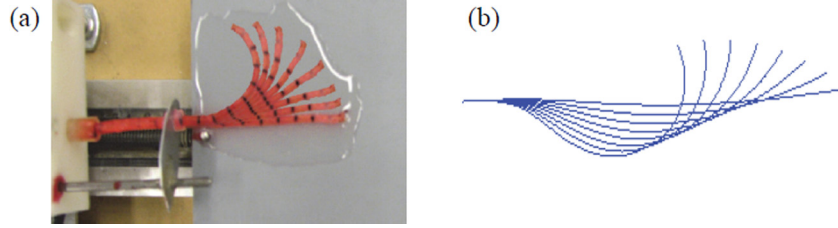


Fig. 6 Overlay of z images (a) taken from calibration process and (b) simulated virtual calibration images using elastic model

The solution of Eq. (18) is given by $[\Gamma^T \otimes \Omega] \text{Vec}(\mathbf{A}) = \text{Vec}(\Phi)$, where \otimes represents Kronecker's matrix product [36] and $\text{Vec}(\mathbf{A}_{v \times w}) = [a_{11} \cdots a_{v1}, a_{12} \cdots a_{v2}, \cdots, a_{1w} \cdots a_{vw}]^T$.

This calibration process will be significantly simplified when the electrode elastic modeling is known. Using the analytic solution of strand placement and the elastic model, the predicted bent shapes of the steerable EAs could be used in the virtual calibration process to replace the real images taken from experiments. z different values of f_i are input to the elastic model, z values of q_1 are solved, and z bent EA shapes are simulated in Fig. 6(b). A number of g imaginary virtual marking points on the EA are taken from the simulated bent shapes. Local tangent angles $\theta_e(s_i, q_{1i})$ of the virtual marking points are easily solved because all the information of the bent shapes is given in the elastic model. Finally, following the same procedures, matrix \mathbf{A} is obtained using Eqs. (17) and (18).

4.3 Robot Path Planning. This section briefly reviews key results about optimal insertion path planning as initially presented in Ref. [27]. The goal of robot path planning is to solve for the optimal robot joint paths that minimize the shape difference between the steerable EAs and the target curve, i.e., scala tympani, during the insertion process. The reason we use shape discrepancy as a measure of good insertion is due to the fact that increased fit between the equilibrium shape of the electrode array and the anatomy results in reduced deformation of the electrode array due to reaction forces with the anatomy. The path planner and electrode array strand placement optimizer try to minimize the discrepancy throughout the insertion process given a limited set of design parameters (actuation strand placement) and a single control variable (actuation strand pull). Based on Refs. [37] and [38], the shape of the scala tympani among all adults is very minimal and can be represented by a unified geometric curve [31]. This path planning is necessary because the optimal strand placement in Sec. 3, although accurate for a given inserted depth d , does not provide how to control the actuation strand, the position and the orientation of the robot during insertion.

Figure 7 shows the schematics of a 4 DoF robot used for electrode insertion. Frames $\{\mathbf{w}\}$, $\{\mathbf{g}\}$, $\{\mathbf{c}\}$ designate the world coordinate system, the robot gripper coordinate system, and the scala tympani coordinate system. \mathbf{c}_{tip} is the point on the scala tympani

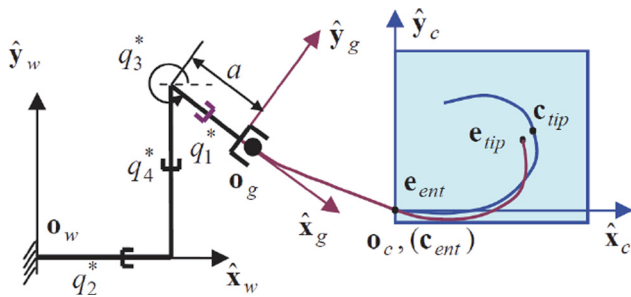


Fig. 7 Schematics of 4 DoF robot with optimization parameters

which corresponds to the tip of the inserted EA \mathbf{e}_{tip} . \mathbf{e}_{ent} is the point on the EA corresponding with \mathbf{c}_{ent} (scala tympani entrance).

The path planning starts with the orientation optimization. For any given q_1 , $\theta_e(s)$ yields a column vector of $\Phi(s, q_1)$ that represents the shape of the bent EAs. Similarly, the shape of scala tympani can be defined as $\tilde{\theta}_c(s)$. The insertion depth d is defined by the arc length of the inserted part of the EA. The objective function for orientation optimization is given by

$$\underset{q_1, q_3}{\text{argmin}} \frac{1}{2} \mathbf{T}^T \mathbf{W}(d) \mathbf{T} \quad (21)$$

where $\mathbf{T} = [\mathbf{S}_c(d) \tilde{\theta}_c - (\mathbf{S}_e(d) \tilde{\theta}_e(q_1) + \mathbf{q}_3(d))]$ and $\mathbf{W}(d)$ is a weight matrix. At insertion depth d , $\mathbf{S}_e(d) = [\mathbf{0}_{u-d} \quad \mathbf{I}_d]$, where \mathbf{I}_d represents the inserted part of EA inside the scala tympani and $\mathbf{0}_{u-d}$ is the uninserted part of the EA. $\mathbf{S}_c(d) = [\mathbf{I}_d \quad \mathbf{0}_{u-d}]$ denotes the length from \mathbf{c}_{ent} to the point \mathbf{c}_{tip} where the tip of the EA should reach. For a given insertion depth d , the optimal bending of the EA q_1^* and the optimal robot base rotation q_3^* are found using (21).

The position of the EA with respect to the scala tympani is constrained by the entrance of the scala tympani \mathbf{c}_{ent} . The optimized result of the EA position and orientation is given by

$$\mathbf{p}_e^*(s, q_1^*, q_3^*) = \mathbf{p}_c(s - (u - d)) - (\mathbf{c}_{\text{ent}} - \mathbf{e}_{\text{ent}}(d, q_1^*, q_3^*)) \quad (22)$$

where $\mathbf{p}_c(s)$ and $\mathbf{p}_e^*(s, q_1^*, q_3^*)$ represent the point of scala tympani and the EA at arc length s in $\{\mathbf{w}\}$, respectively, and $(u - d) \leq s \leq u$. The optimized gripper position is solved by

$$\mathbf{o}_g^*(q_1^*, q_3^*) = \mathbf{p}_e^*(0, q_1^*, q_3^*) \quad (23)$$

The inverse kinematics of the planar robot is then solved as shown in Fig. 7. Detailed derivations and examples were given in Ref. [27].

4.4 Optimization Algorithm. The analytical solution solves for the strand placement inside the steerable EA for a given target curve length (insertion depth) d . However, there are two remaining issues that need investigation.

First, the analytical solution solves the strand placement using the elastic model of the EA. In each segment, the strand placement is represented by the location of strand. Connecting all these strand locations results in a continuous curve with the assumption that the total number of layers n is large enough and there is no sudden jump of the strand location between two adjacent layers. Nevertheless, this analytic representation of strand poses difficulty for electrode fabrication.

Second, the strand placement from analytic solution aims to find the desired strand placement for a given insertion depth, i.e., the full insertion depth. At any other given insertion depth d , the robot path planning algorithm minimizes the shape difference between the bent EAs and the target curve. It is evident that the shape of the bent EAs may not perfectly match the target curve due to the constraints of robot joint limits.

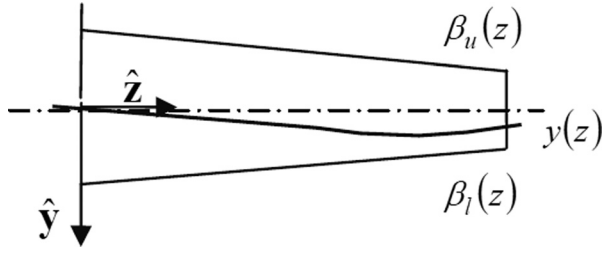


Fig. 8 A strand placement using k th order polynomial expression

An alternative to analytical solution is to represent the strand inside the steerable EA using the following k th order polynomial

$$y(z) = \sum_{\alpha=0}^k c_{\alpha} z^{\alpha} = \mathbf{c}^T \mathbf{z}, \quad \beta_l(z) \leq y(z) \leq \beta_u(z) \quad (24)$$

where $\beta_u(z)$ and $\beta_l(z)$ are the upper and lower bounds of the EAs as shown in Fig. 8. $\mathbf{c} = [c_k, c_{k-1}, \dots, c_0]^T$ and $\mathbf{z} = [z^k, z^{k-1}, \dots, z^0]^T$. This analytic expressed shape of the strand placement makes the fabrication process easier and practical compared to the discretely connected shape of the strand placement results from the analytical solution.

To quantify the shape differences between the target curve and the bent EAs, we propose the simulated average angle variation at insertion depth d , which is defined by

$$\bar{\theta}(d, q_{\gamma}^*) = \frac{1}{d} \int_0^d \left| \theta_c(s) - \theta_e(u-d+s, q_{\gamma}^*) \right| ds \quad (25)$$

where $\bar{\theta}(d, q_{\gamma}^*)$, ($\gamma = 1, 2, 3, 4$) is the average angle difference between the inserted part of the bent EAs and the scala tympani curve at insertion depth d when using the optimized parameters q_{γ}^* for joint values. For the whole insertion process, the total simulated average angle variation is defined by

$$\bar{\theta}_t = \frac{1}{2} \sqrt{\int_0^u \left[\bar{\theta}(d, q_{\gamma}^*) \right]^T \bar{\theta}(d, q_{\gamma}^*) dd} \quad (26)$$

Using (24)–(26), a nonlinear optimization problem with nonlinear constraints is formulated as shown below

$$\arg \min_{\mathbf{c}} \bar{\theta}_t = \frac{1}{2} \sqrt{\int_0^u \left[\bar{\theta}(d, q_{\gamma}^*) \right]^T \bar{\theta}(d, q_{\gamma}^*) dd} \quad (27)$$

subject to

$$\beta_l(z) \leq y(z) \leq \beta_u(z) \quad (28)$$

We solve for the coefficients of the strand placement \mathbf{c} that minimize the total simulated average angle variation throughout the whole insertion process. Figure 9 shows the flow chart of the optimization algorithm.

An initial strand placement \mathbf{c}_0 and a small allowable error ε in total average angle mismatch are set. Using this strand placement, we virtually simulate the calibration process using the elastic model to obtain the electrode characteristic matrix \mathbf{A} . This process is detailed in Sec. 4.2 and Fig. 10.

Once the electrode characteristic matrix \mathbf{A} is obtained, the insertion module will simulate the insertion process using this electrode to solve the total average angle variations. Section 4.3 and Eqs. (25) and (26) describe the insertion simulation in detail and Fig. 11 shows the flow chart.

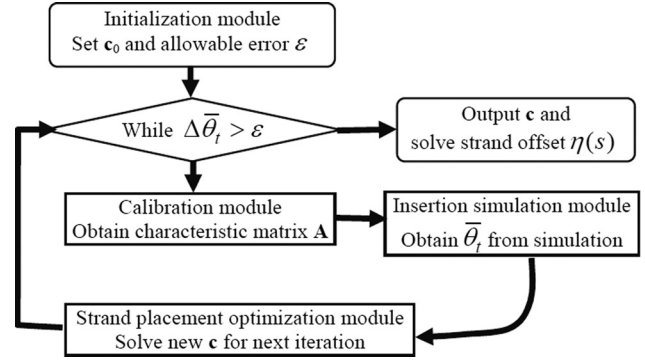


Fig. 9 Flow chart of optimization algorithm

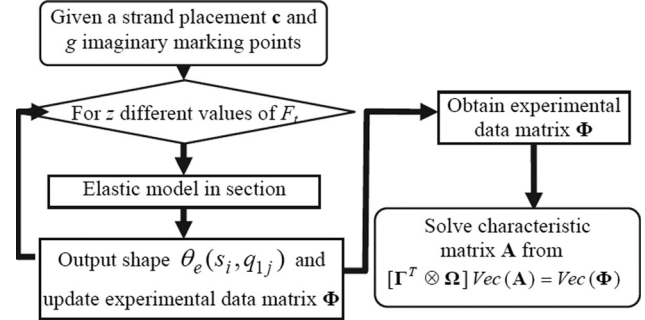


Fig. 10 Detailed flow chart of virtual calibration module

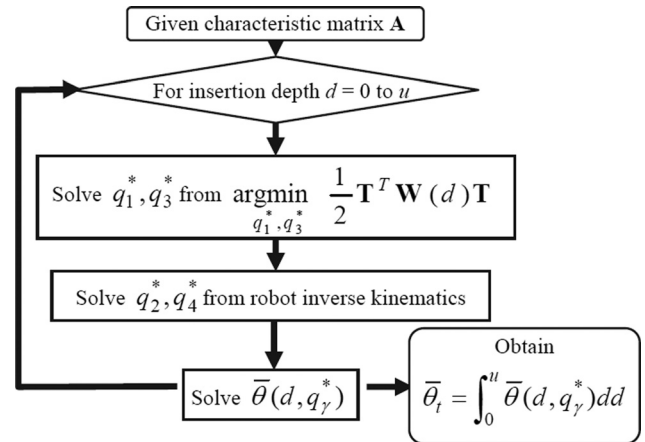


Fig. 11 Detailed flow chart of insertion simulation module

The strand optimization algorithm simplifies optimization problem by converting the nonlinear constraints into a set of linear constraints and solves the problem using the active set algorithm [39]. For the constraints in Eq. (28), at any layer i of the EA, $z = \frac{i}{n}u$ and the following equation hold:

$$\begin{cases} -\sum_{\alpha=0}^k c_{\alpha} \left(\frac{i}{n}u\right)^{\alpha} \leq -\beta_l\left(\frac{i}{n}u\right) \\ \sum_{\alpha=0}^k c_{\alpha} \left(\frac{i}{n}u\right)^{\alpha} \leq \beta_u\left(\frac{i}{n}u\right) \end{cases} \quad (29)$$

In matrix form, (29) is equivalent to

$$\mathbf{Uc} \leq \mathbf{B} \quad (30)$$

where

$$\mathbf{U} = \begin{bmatrix} -\mathbf{I} \\ \mathbf{I} \end{bmatrix} \begin{bmatrix} 1 & \cdots & \left(\frac{1}{n}u\right)^{k-1} & \left(\frac{1}{n}u\right)^k \\ 1 & \cdots & \left(\frac{2}{n}u\right)^{k-1} & \left(\frac{2}{n}u\right)^k \\ \vdots & \vdots & \vdots & \vdots \\ 1 & \cdots & u^{k-1} & u^k \end{bmatrix}, \quad \mathbf{B} = \begin{bmatrix} -\mathbf{B}_l \\ \mathbf{B}_u \end{bmatrix}$$

$$\mathbf{B}_l = \left[\beta_l \left(\frac{1}{n}u\right) \quad \beta_l \left(\frac{2}{n}u\right) \quad \cdots \quad \beta_l u \right]^T$$

and

$$\mathbf{B}_u = \left[\beta_u \left(\frac{1}{n}u\right) \quad \beta_u \left(\frac{2}{n}u\right) \quad \cdots \quad \beta_u u \right]^T$$

The optimal strand placement coefficients \mathbf{c} are solved using the active set algorithm via *fmincon* MATLAB function. The search space of possible strand placements is constrained. We believe that the analytical solution is close enough to the optimal strand placement throughout the whole insertion process. Therefore, we will use the analytical solution from Sec. 4.1 as the initial condition to search for the optimized strand placement. Since the search space is small and limited by the electrode bounds, the local minimal can be treated as the final optimal solution.

5 Simulation Results

The simulation results in this section use an EA with a rectangular cross section to match the electrode used in Sec. 4.

5.1 Electrode Bending Based on Elastic Modeling. The elastic model was implemented using MATLAB. For any arbitrary determined strand placement, it simulated a group of bent shapes of the steerable EA. Figure 12(a) shows a given strand placement. The solid black line shows the strand with an offset respect to the red centerline. The electrode has a rectangular cross section where the width is $w = 3$ mm, the depth is $h = 6$ mm, and length $u = 75$ mm. The blue outer line shows the geometry of the EA in y - z plane. Figure 12(b) shows five simulated bent shapes for five different applied forces f_i . The internal friction force per unit length is $\alpha_\mu \approx 0.01$ N/mm.

5.2 Strand Placement Results From Analytical Solution. Our earlier work [18,27,28] used the scala tympani model in Refs. [37,38,40] as the target curve. This model of the scala tympani curve is composed from two curves and it is not first-order continuous at the transition between the two curves. This discontinuity generates a discontinuity in the strand placement.

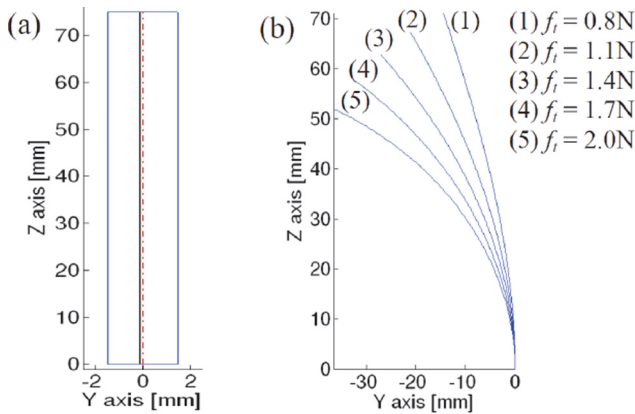


Fig. 12 (a) An arbitrary given strand placement and (b) bent shapes of the steerable electrode array with the strand placement in (a)

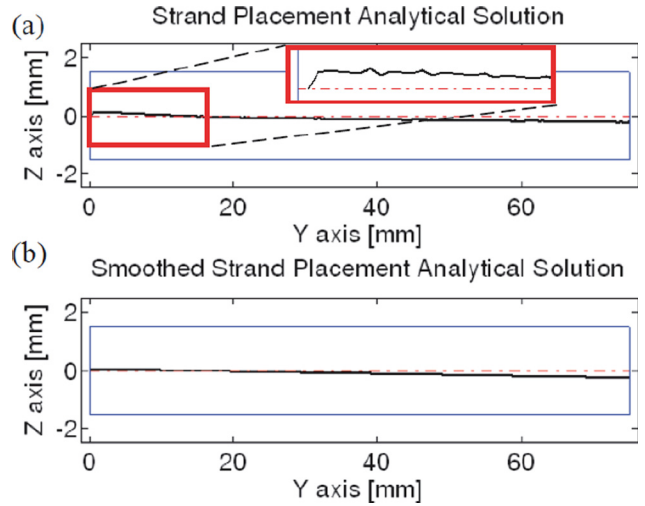


Fig. 13 (a) Solved strand placement from analytical solution and (b) smoothed strand placement based on (a)

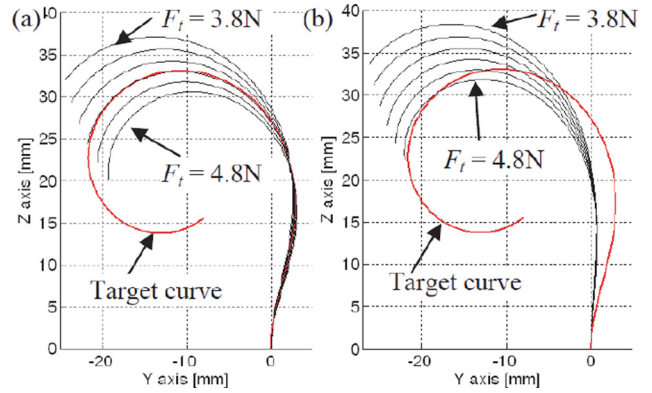


Fig. 14 Modified target curve with simulated bent electrode shapes (a) using unsmoothed strand placement in Fig. 13(a) and (b) using smoothed strand placement in Fig. 13(b)

Therefore, we slightly modified the target curve to enforce first-order differentiability

$$R(\varphi) = \lambda\tau(1 - \omega \log(\varphi - \varphi_0)) \quad (31)$$

where $\varphi \in (10.3 \text{ deg}, 375.3 \text{ deg})$, $\lambda = 4$ is a scale factor, τ , ω , and φ_0 are given in Refs. [34] and [37]. Equation (31) has first-order continuity and the analytical solution of the strand placement will generate a strand shape shown in Fig. 13(a). The desired strand placement shown in Fig. 13(a) is represented by connecting all the strand locations at each segment directly, which is not necessarily smooth. Then, we smoothed analytical solution using a least-square straight line fit to all the strand locations at each segment. The coefficients of the straight line are given by $\mathbf{c} = [-0.004114, 0.040207]^T$ and the smoothed straight line is shown in Fig. 13(b).

Using the solved strand placement in Fig. 13(a), a group of simulated electrode bent shapes are overlaid on the target curve (31) in Fig. 14(a). The bent EA fits the target curve well when $f_i = 4.4$ N. Similarly, a group of simulated electrode bent shapes are overlaid in Fig. 14(a) using the smoothed strand placement in Fig. 13(b).

Using the analytical solution of the strand placement, an insertion simulation is carried out using the following conditions:

The insertion depth starts from $d = 1$ mm and ends at $d = 75$ mm with an increment of 1 mm. The applied force ranges from $f_i = 1$ N to $f_i = 4.5$ N with an increment of 0.25 N. The biggest

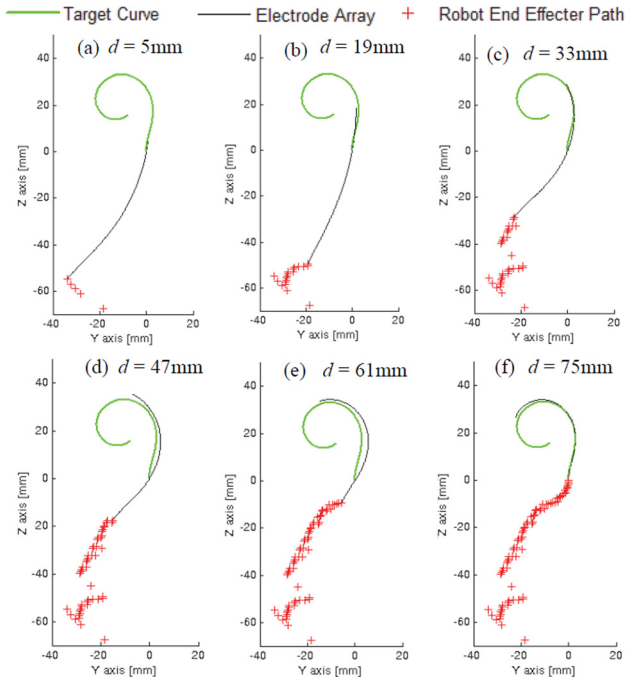


Fig. 15 Simulation using unsmoothed analytical solution of strand placement

robot base rotation angle is $q_3 = 4$ deg and the smallest is $q_3 = -40$ deg with a step of 2 deg.

Figure 15 shows the insertion simulation results using the strand placement in Fig. 13(a). The total average angle variation in Eq. (26) is calculated $\bar{\theta}_t = 24.180$ deg. Note that Fig. 15(f) shows a perfect shape match at insertion depth $d = 75$ mm because the analytical solution of the strand placement is solved based on this particular insertion depth. Although the simulation shows that using the strand placement of the analytical solution achieves pretty good shape match during insertions, the wiggled shape of the strand placement in Fig. 13(a) is almost impossible to achieve in fabrications. In contrast, the simulation using the linearized strand placement in Fig. 13(b) gives a total average angle variation $\bar{\theta}_t = 20.111$ deg.

5.3 Strand Placement Optimization Algorithm. Compared to the results using the strand placement from analytical solution, which perfectly matches the target curve shape at the full insertion depth, the strand placement optimization algorithm solves for an optimized strand placement that minimizes the shape discrepancies between the bent electrode shapes and the target curve throughout the whole insertion process. Although higher order polynomial representation in Eq. (24) gives better results of strand placement, considering the feasibility of fabrication, we simulated two cases where we assumed the strand placement takes the shape of a linear equation and a second-order polynomial.

The simulation conditions remain the same as in Sec. 5.2 and the only difference is the strand placement inside the electrode. Since the gradient method is sensitive to the initial conditions, we chose the smoothed strand placement as the initial condition from the analytical solution which is a straight line with coefficients $\mathbf{c} = [-0.004114, 0.040207]^T$.

The solved coefficients of the optimized linear equation are $\mathbf{c} = [-0.004691, 0.062092]^T$. Figure 16(a) shows the optimized strand placement inside the electrode. The calculated total simulated average angle variation in Eq. (26) is $\bar{\theta}_t = 19.677$ deg.

When optimizing the strand placement using a second-order polynomial representation, the initial condition is also set the same as the analytical solution which is \mathbf{c}

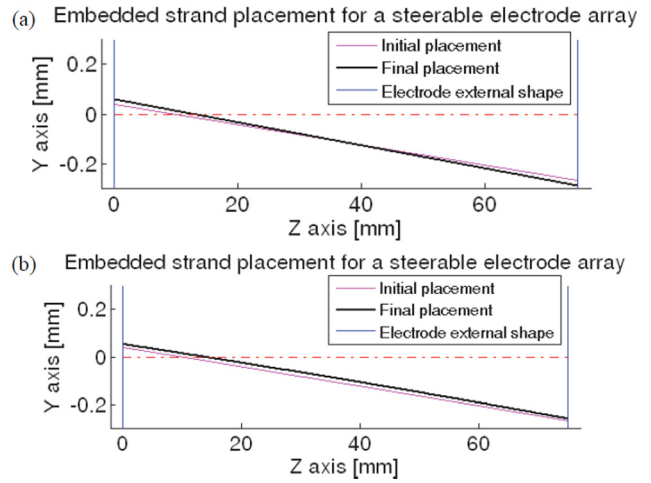


Fig. 16 Optimization algorithm results (a) linear strand placement and (b) nonlinear strand placement

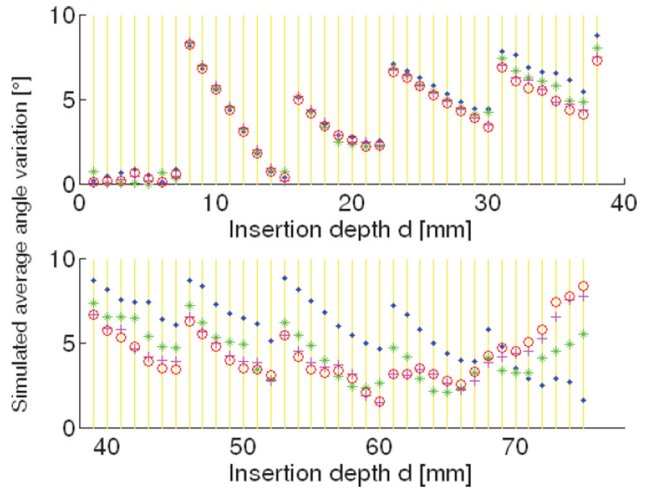


Fig. 17 Comparison of four insertion simulation results, AS, analytical solution; OA, optimization algorithm; SP, strand placement

$= [0, -0.004114, 0.040207]^T$. The optimized coefficients are $\mathbf{c} = [-0.0000046, -0.003839, 0.052944]^T$. Figure 16(b) shows the optimized strand placement inside the electrode. The calculated total simulated average angle variation in Eq. (26) is $\bar{\theta}_t = 19.470$ deg.

In order to compare different insertion simulation results, Fig. 17 shows the simulated average angle variation defined by Eq. (25) of each insertion. The analytical solution (blue dots) achieves the best match at full insertion depth ($d = 75$ mm) but is the worst fit in the insertion range $d \in [30, 70]$ mm compared to others. The smoothed strand placement from analytical solution (green stars) fits better in the middle portion of insertion compared to unsmoothed strand placement. In general, using optimization algorithm maintains a better shape fit throughout the whole insertion process. The second-order strand placement is comparable to the linear strand placement.

5.4 Global Search Using Optimization Algorithm. Further, to validate that the optimized strand placement is close to the global optimum, we chose 25 different initial conditions for the strand placement as shown in Fig. 18. Five equidistant points were selected on both ends of the electrode. The 25 initial strand placements connect any combination of two points on either end.

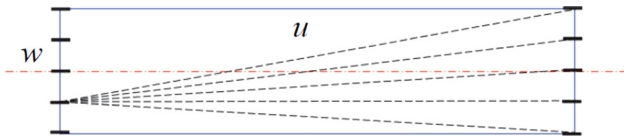


Fig. 18 Selection of initial conditions for global search

Using the optimization algorithm, 25 local optimal strand placements have been calculated for both linear and nonlinear cases. Among all 25 linear cases, two initial conditions generate better results than the results shown in Sec. 5.3. For the nonlinear cases, no initial conditions can result in better strand placement than the one shown in Sec. 5.3. Table 2 shows the detailed results. Therefore, the optimal results solved by using the initial condition from the analytical strand placement is close enough to the global optimum.

6 Experimental Results

Two experiments have been conducted to validate our proposed elastic model and optimization algorithms.

6.1 Validation of the Elastic Statics Model. We fabricated a steerable electrode with $w = 3$ mm, $h = 6$ mm, and length $u = 75$ mm. The desired strand placement is shown in Fig. 12(a). The strand is made of Kevlar with $100 \mu\text{m}$ outer diameter, which can be replaced by NiTi wires for clinical tests. Considering the complexity of placing high-order strand curve, a simple linear strand placement is used. We controlled the Y-Z plane strand placement using two customized slides and strong cable tension to keep the strand in Y-Z plane during the molding of the electrode array.

In order to compare the simulated bent shapes of the steerable EA, we overlaid the simulation results onto the real bent shapes of the EA. Figure 19 shows the overlaid results. Each subfigure is an overlay of three images with different values of f_i .

The actual bent shapes of the EA fit the predicted bent shapes pretty well. Small errors have been discovered due to three experimentally determined parameters: the internal friction coefficient α_f , the Young's modulus of the silicone E , and the actual strand placement w_{iy} after molding. The uncertainties in these parameters affect the simulation results.

We include error bounds in all three parameters separately to compare with experimental results. Figure 20(a) shows a simulated bent shape of the EA with $\pm 5\%$ error bounds on the internal friction. These error bounds result in very small electrode shape deviation compared to the effects of $\pm 5\%$ error bounds of the Young's modulus as shown in Fig. 20(b). In addition, a misalignment of the actual strand from the desired theoretical placement leads to error in the actual bending shapes of the EA. Image segmentation has been implemented using the fabricated EA to localize where the actual strand is and to use the strand placement in the statics simulation. Figure 21 shows the segmentation process

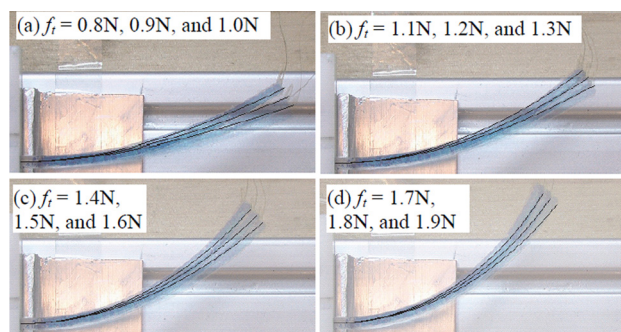


Fig. 19 Overlay of simulation results onto bent electrode arrays

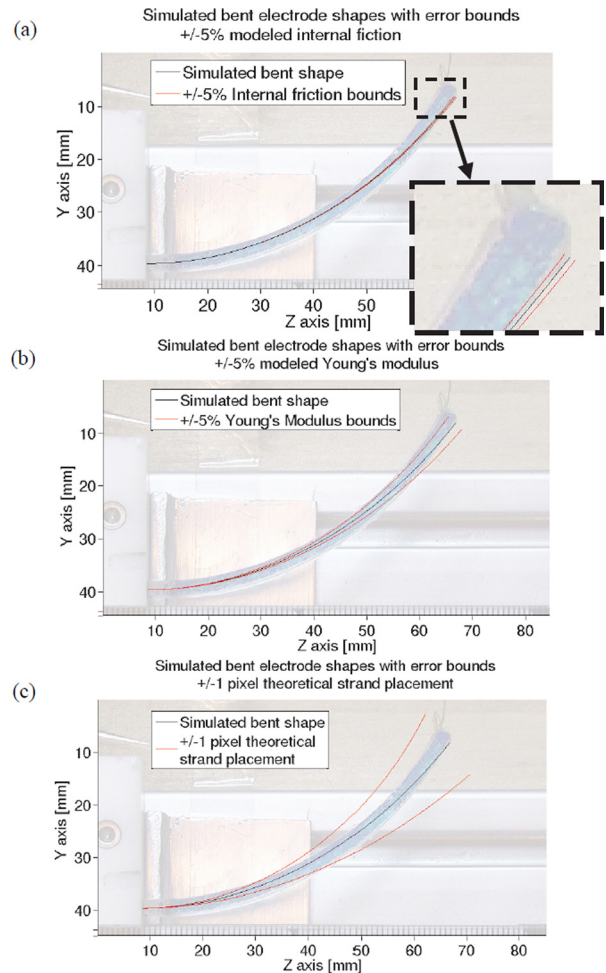


Fig. 20 Simulated bent electrode shapes with error bounds (a) $\pm 5\%$ modeled internal friction, (b) $\pm 5\%$ measured Young's modulus, (c) Simulated bent electrode shapes with ± 1 pixel segmentation error bounds.

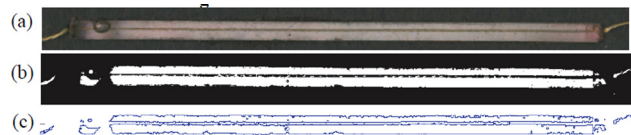


Fig. 21 Segmentation of fabricated electrode array with designed strand placement (a) raw image, (b) BW image, and (c) segmented image

of the fabricated EA. The segmentation results show that the actual placement of the strand is very close to the designed strand placement Fig. 12(a). However, ± 1 pixel error is noticeable. Considering the diameter of the strand $d_w = 0.35$ mm, the actual offset of 1 pixel corresponds 21% error in locating the strand (due to the resolution of our scan). Figure 20(c) shows the simulated bent shape of the EA with ± 1 pixel error bounds of the strand placement. This is assuming the worst case where all layers and the strand are offset +1 or -1 pixel. The two red bent shapes demonstrate that the experiment we did resulted in a bent electrode with a discrepancy from our nominal statics model that is smaller than the experimental errors. Hence, Figs. 19 and 20 indeed validate the elastic model of Sec. 3.

6.2 Insertion Experiments Using Optimal Insertion Algorithm. The second validation experiment compares the insertions of an optimized steerable electrode versus a

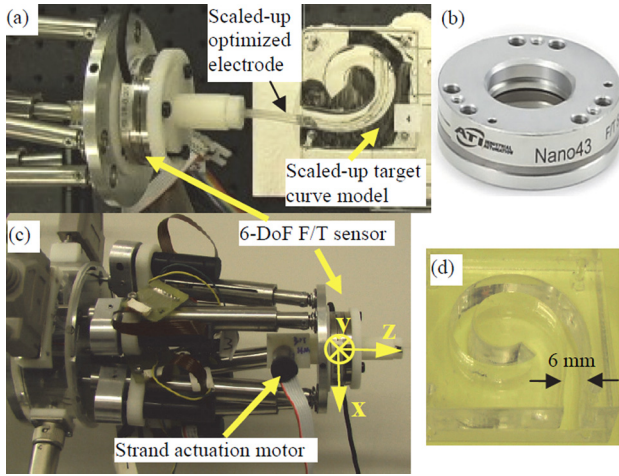


Fig. 22 (a) Experimental setup, (b) 6-DoF F/T sensor, (c) parallel robot with strand actuation motor and F/T sensor coordinate systems, and (d) scaled-up target curve model

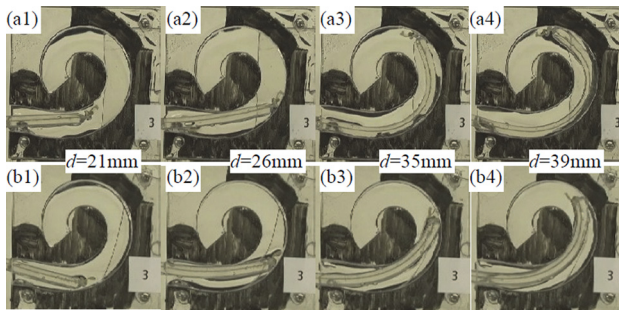


Fig. 23 Comparison of insertion images using (a) 1 DoF non-steerable (straight) electrode and (b) 4 DoF steerable electrode

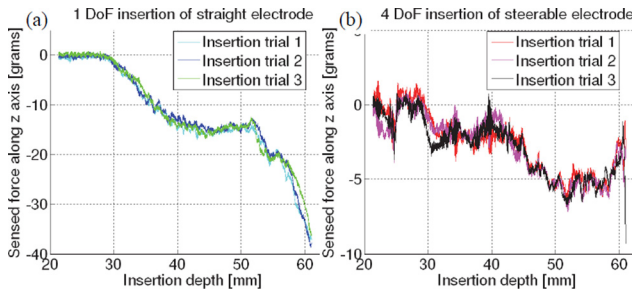


Fig. 24 Comparison of insertion forces using (a) 1 DoF non-steerable (straight) electrode and (b) 4 DoF steerable electrode

nonsteerable (straight) electrode. Table 2 shows that a linear strand placement is a good compromise between performance and fabrication simplicity. The experimental setup shown in Fig. 22 used a six DoF parallel robot designed for real-size electrode insertions [41]. A six DoF force and torque sensor (ATI Nano 43) and a strand actuation motor were added. A scaled-up target curve based on Eq. (31) was fabricated in an acrylic plate.

When inserting steerable EAs, the parallel robot follows the optimized path, as shown in Fig. 15. Nonsteerable electrode insertions only require single axis movement of the robot. For each insertion, three trials are carried out to show repeatability. 100% glycerin is injected into the cochlea model for lubrication.

The robot in Fig. 22 was designed for a 1:1 real-size electrode. Due to workspace limitations, we validated intermediate depth

insertions ($d = 21$ to $d = 61$ mm). Figure 23 and supplemental material² show the insertion of the straight electrode and the insertion of the optimized steerable electrode. The optimized steerable electrode bends toward the inner wall of the target curve as predicted in the simulation, Fig. 15. Insertion forces are quantified and the forces along insertion direction (z axis in Fig. 22). Figure 24 shows that the optimized steerable electrode reduced the insertion forces by 82%.

7 Conclusion

This paper presented a framework for the static modeling, optimal design, and insertion path planning of steerable EAs. These steerable EAs have an embedded actuation strand inside a flexible medium. A statics model was presented using the finite layer method and a forward recursion that allows a closed-form solution for the desired actuation strand placement in order to bend the electrode at a given desired shape. This method was used in conjunction with a virtual calibration algorithm followed by optimal insertion path planning. The results showed that strand placement based on the closed-form recursive solution is not sufficient for an optimal match between the shapes of the EA and the cochlea target curve. This method provides a very good match only at a specific insertion depth. A strand placement optimization algorithm was derived using a constrained optimization framework that minimizes the total shape discrepancy between the bending EA and the target curve throughout the whole insertion process. These models were simulated and verified by experiments showing 82% reduction in the insertion force.

Nomenclature

- u = scalar representing the total length of the electrode array
- d_w = scalar representing the diameter of the actuation strand
- n = integer designating total number of electrode segments after discretization
- i = subscript index designating the segment number from the base of the electrode ($i = 1 \dots n$)
- E = constant denoting Young's modulus of electrode array
- A_i = scalar, representing cross sectional area of segment i
- $\{\mathbf{o}_i\}$ = local coordinate system of segment i , see Fig. 3
- $\hat{\mathbf{x}}_i$ = normalized directional vector, representing the local x axis of segment i
- (i) \mathbf{w}_i = point denoting the strand location of segment i in coordinate system $\{\mathbf{o}_i\}$, see Figs. 3 and 4
- $\mathbf{a}_{i+1/i}$ = vector from \mathbf{c}_i to \mathbf{w}_{i+1} , $\{\mathbf{o}_i\}$, see Figs. 3 and 4
- \mathbf{C}_i = compliance matrix of segment i
- $\overline{\mathbf{p}_i \mathbf{p}_{i+1}}$ = arc length between point \mathbf{p}_i and \mathbf{p}_{i+1}

References

- [1] Wardrop, P., Whinney, D., Rebscher, S. J., Luxford, W., and Leake, P., 2005, "A Temporal Bone Study of Insertion Trauma and Intracochlear Position of Cochlear Implant Electrodes. II: Comparison of Spiral Clarion and HiFocus II Electrodes," *Hear. Res.*, **203**, pp. 68–79.
- [2] Wardrop, P., Whinney, D., Rebscher, S. J., Roland, J. J. T., Luxford, W., and Leake, P. A., 2005, "A Temporal Bone Study of Insertion Trauma and Intracochlear Position of Cochlear Implant Electrodes. I: Comparison of Nucleus Banded and Nucleus Contour(TM) Electrodes," *Hear. Res.*, **203**, pp. 54–67.
- [3] Adunka, O., Gstoettner, W., Hambek, M., Unkelbach, M. H., Radeloff, A., and Kiefer, J., 2004, "Preservation of Basal Inner Ear Structures in Cochlear Implantation," *ORL*, **66**, pp. 306–312.
- [4] Adunka, O., Kiefer, J., Unkelbach, M. H., Lehnert, T., and Gstoettner, W., 2004, "Development and Evaluation of an Improved Cochlear Implant Electrode Design for Electric Acoustic Stimulation," *Laryngoscope*, **114**, pp. 1237–1241.
- [5] Eshraghi, A. A., Yang, N. W., and Balkany, T. J., 2003, "Comparative Study of Cochlear Damage With Three Perimodiolar Electrode Designs," *Laryngoscope*, **113**, pp. 415–419.

²http://research.vuse.vanderbilt.edu/arma/Media/JMR_cochlea1.wmv [42]

- [6] Maeno, T., Hiromitsu, S., and Kawai, T., 2000, "Control of Grasping Force by Detecting Stick/Slip Distribution at the Curved Surface of an Elastic Finger," IEEE International Conference on Robotics and Automation, San Francisco, CA, USA, p. 3895.
- [7] Gstoettner, W., Plenk, H., Jr., Franz, P., Hamzavi, J., Baumgartner, W., Czerny, C., and Ehrenberger, K., 1997, "Cochlear Implant Deep Electrode Insertion: Extent of Inertial Trauma," *Acta Oto-Laryngol.*, **117**, pp. 274–277.
- [8] Roland, J. T. J., 2005, "A Model for Cochlear Implant Electrode Insertion and Force Evaluation: Results With a New Electrode Design and Insertion Technique," *Laryngoscope*, **15**, pp. 1325–1339.
- [9] Fishman, A., Roland, J. T., Jr., Alexiades, G., Mierzwinski, J., and Cohen, N. L., 2003, "Fluoroscopically Assisted Cochlear Implantation," *Otol. Neurotol.*, **24**, pp. 882–886.
- [10] Leob, G. E., Peck, R. A., and Smith, D. W., 1995, "Microminiature Molding Techniques for Cochlear Electrode Arrays," *J. Neurosci. Methods*, **63**, pp. 85–92.
- [11] Adunka, O., Kiefer, J., Unkelbach, M., and Lehnert, T., 2004, "Development and Evaluation of an Improved Cochlear Implant Electrode Design for Electric Acoustic Stimulation," *Laryngoscope*, **114**, pp. 1237–1241.
- [12] Kha, H. N., Chen, B. K., Clark, G. M., and Jones, R., 2004, "Stiffness Properties for Nucleus Standard Straight and Contour Electrode Arrays," *Med. Eng. Phys.*, **26**, pp. 677–685.
- [13] Chen, B. K., Clark, G. M., and Jones, R., 2003, "Evaluation of Trajectories and Contact Pressures for the Straight Nucleus Cochlear Implant Electrode Array—A Two Dimensional Application of Finite Element Analysis," *Med. Eng. Phys.*, **25**, pp. 141–147.
- [14] Frijns, J. H. M., Briarie, J. J., and Grote, J. J., 2001, "The Importance of Human Cochlear Anatomy for the Results of Modiolus-Hugging Multi-Channel Cochlear Implants," *Otol. Neurotol.*, **22**, pp. 340–349.
- [15] Wang, J., Gulari, M., and Wise, K. D., 2005, "An Integrated Position-Sensing System for a MEMS-Based Cochlear Implant," Electron Devices Meeting, IEDM Technical Digest, IEEE International, pp. 121–124.
- [16] Wang, J., Gulari, M. N., and Wise, K. D., 2006, "A Parylene-Silicon Cochlear Electrode Array With Integrated Position Sensors," Engineering in Medicine and Biology Society, EMBS 06, 28th Annual International Conference of the IEEE, pp. 3170–3173.
- [17] Zhang, J., Bhattacharyya, S., and Simaan, N., 2009, "Model and Parameter Identification of Friction During Robotic Insertion of Cochlear-Implant Electrode Arrays," IEEE International Conference on Robotics and Automation, ICRA '09, pp. 3859–3864.
- [18] Zhang, J., Xu, K., Simaan, N., and Manolidis, S., 2006, "A Pilot Study of Robot-Assisted Cochlear Implant Surgery Using Steerable Electrode Arrays," *Med. Image Comput. Assist. Interv.*, **9**, part I, pp. 33–40.
- [19] Hussong, A., Rau, T., Ortmaier, T., Heimann, B., Lenarz, T., and Majdani, O., 2009, "An Automated Insertion Tool for Cochlear Implants: Another Step Towards Atraumatic Cochlear Implant Surgery," *Int. J. Comput. Assist. Radiol. Surg.*, **5**(2), pp. 163–171.
- [20] Rau, T., Hussong, A., Leinung, M., Lenarz, T., and Majdani, O., 2009, "Automated Insertion of Preformed Cochlear Implant Electrodes: Evaluation of Curling Behaviour and Insertion Forces on an Artificial Cochlear Model," *Int. J. Comput. Assist. Radiol. Surg.*, **5**(2), pp. 173–181.
- [21] Suzumori, K., Iikura, S., and Tanaka, H., 1991, "Flexible Microactuator for Miniature Robots," IEEE International Conference on Robotics and Automation, pp. 204–209.
- [22] Chen, B., Kha, H., and Clark, G., 2006, "Development of a Steerable Cochlear Implant Electrode Array," 3rd Kuala Lumpur International Conference on Biomedical Engineering, pp. 607–610.
- [23] Giesler, D. C., 1998, *From Sound to Synapse: Physiology of the Mammalian Ear*, Oxford University Press, New York.
- [24] Robinson, G., and Davies, J., 1999, "Continuum Robots—A State of the Art," IEEE International Conference on Robotics and Automation, pp. 2849–2853.
- [25] Chirikjian, G., and Burdick, J., 1995, "Kinematically Optimal Hyper-Redundant Manipulator Configurations," *IEEE Trans. Rob. Autom.*, **11**, pp. 794–806.
- [26] Webster, R. J., Romano, J. M., and Cowan, N. J., 2009, "Mechanics of Precurved-Tube Continuum Robots," *IEEE Trans. Rob.*, **25**, pp. 67–78.
- [27] Zhang, J., Roland, J. T., Manolidis, S., and Simaan, N., 2009, "Optimal Path Planning for Robotic Insertion of Steerable Electrode Arrays in Cochlear Implant Surgery," *J. Med. Devices*, **3**, p. 011001.
- [28] Zhang, J., Wei, W., Manolidis, S., Roland, J., and Simaan, N., 2008, "Path Planning and Workspace Determination for Robot-Assisted Insertion of Steerable Electrode Arrays for Cochlear Implant Surgery," *Med. Image Comput. Assist. Interv.*, **11**(2), pp. 692–700.
- [29] Dupont, P. E., Lock, J., Itkowitz, B., and Butler, E., 2010, "Design and Control of Concentric-Tube Robots," *IEEE Trans. Rob.*, **26**(2), pp. 209–225.
- [30] Rucker, D. C., Webster, R. J., Chirikjian, G. S., and Cowan, N. J., 2010, "Equilibrium Conformations of Concentric-Tube Continuum Robots," *Int. J. Rob. Res.*, **29**(10), pp. 1263–1280.
- [31] Lyons, L. A., Iii, R. J. W., and Alterovitz, R., 2009, "Motion Planning for Active Cannulas," IEEE/RSJ International Conference on Intelligent Robots and System, pp. 801–806.
- [32] Webster, R. J. I., Cowan, N. J., Chirikjian, G., and Okamura, A. M., 2006, "Nonholonomic Modeling of Needle Steering," *Int. J. Rob. Res.*, **25**(5–6), pp. 509–525.
- [33] Alterovitz, R., and Goldberg, K., 2010, "Algorithms for Steerable Needles Using Inverse Kinematics," *Int. J. Rob. Res.*, **29**(7), pp. 789–800.
- [34] Glozman, D., and Shoham, M., 2007, "Image-Guided Robotic Flexible Needle Steering," *IEEE Trans. Rob.*, **23**(3), pp. 459–467.
- [35] Chirikjian, G. S., and Burdick, J. W., 1994, "A Modal Approach to Hyper-Redundant Manipulator Kinematics," *IEEE Trans. Rob. Autom.*, **10**, pp. 343–354.
- [36] Graham, A., 1981, *Kronecker Products and Matrix Calculus With Applications*, Ellis Horwood Limited, New York.
- [37] Cohen, L., Xu, J., Xu, S. A., and Clark, G. M., 1996, "Improved and Simplified Methods for Specifying Positions of the Electrode Bands of a Cochlear Implant Array," *Am. J. Otol.*, **17**, pp. 859–865.
- [38] Ketten, D. R., Skinner, M. W., Wang, G., Vannier, M. W., Gates, G. A., and Neely, J. G., 1998, "In Vivo Measures of Cochlear Length and Insertion Depth of Nucleus Cochlear Implant Electrode Arrays," *Ann. Otol. Rhinol. Laryngol. Suppl.*, **175**, pp. 1–16.
- [39] Nocedal, J., and Wright, S. J., 2006, *Numerical Optimization*, Springer, New York.
- [40] Yoo, S. K., Wang, G., Rubinstein, J. T., Skinner, M. W., and Vannier, M. W., 2000, "Three-Dimensional Modeling and Visualization of the Cochlea on the Internet," *IEEE Trans. Inf. Technol. Biomed.*, **4**, pp. 144–151.
- [41] Zhang, J., Manolidis, S., Roland, T. J., and Simaan, N., 2008, "Path Planning and Workspace Determination for Robot-Assisted Insertion of Steerable Electrode Arrays for Cochlear Implant Surgery," International Conference on Medical Image Computing and Computer-Assisted Intervention (MICCAI'2008).
- [42] See supplementary material at E-JMROA6. The video shows a comparison of the insertion process of a straight electrode and a steerable electrode with optimized strand placement and steerable insertion path planning. The video is available at: http://research.vuse.vanderbilt.edu/arma/Media/JMR_cochlea1.wmv.